Jestr

Journal of Engineering Science and Technology Review 15 (2) (2022) 167 - 176

JOURNAL OF
Engineering Science and Technology Review

Research Article

www.jestr.org

Structural Stability Analysis of Concrete Lining in the Shaft–Tunnel Intersection Area of the Long-Distance Tunnel

Liu Xiaolin[1], Yu Yuanquan[2,*], Yang Tianchun[2], Guan Ling[1] and Yu Congshui[1]

[1]*Chongqing Institute of Foreign Studies, Chongqing 401120, China*
[2]*Beijing Urban Construction Design & Development Group Co., Limited, Beijing 100037, China*

Received 17 February 2022; Accepted 30 May 2022

Abstract

Deformation and stress distribution at the shaft–tunnel intersection (STI) area is more complicated than those of the ordinary part of the tunnel. However, studies on structural stability analysis of tunnels in this area are limited. Vertical deformation, horizontal convergence, and maximum stress in STI areas were investigated via laboratory testing and numerical simulation to evaluate the stability of the STI area accurately and facilitate the implementation of corresponding treatment measures based on a long-distance operation tunnel in Chongqing, China. Primary support and surrounding rock stability in the STI area were analysed by combining the two evaluation indexes of allowable deformation and safety factors. Results show that the maximum vertical deformation is less than 5 mm and the horizontal convergence is less than 2 mm when the design value of 24 cm is used for the initial support. The maximum tensile stresses of the left and right STI areas demonstrate a tensile strength of 71.3% and 69.0%, respectively. The primary support strength is appropriately exerted and the structure is still safe. The concrete primary support with a thickness of 24 cm can ensure that the minimum safety factor of the STI area reaches 5.04, which is larger than the specified value and presents a large surplus. In addition, the average thickness of the actual primary support reaches approximately 32 cm, and the minimum safety factor of the actual STI area will be greater than 5.04. This study can provide a reference for the structural design and construction of the STI area for a similar long-distance tunnel.

Keywords: Long-distance tunnel, Shaft–Tunnel intersection area, Concrete lining, Numerical simulation, Structural stability

1. Introduction

The increase in length and scale of tunnel construction due to rapid economic and infrastructure development in recent years has led to the emergence of super long-distance tunnels of over 6 km [1-4]. Vertical shafts in long-distance tunnels are generally used to improve internal ventilation conditions of tunnels because of their advantages of the short construction period, high efficiency, mature technology, and low operation and maintenance costs [3]. Ventilation shafts based on shaft excavation technology [5, 6], ventilation shaft design technology of flue gas characteristics [7], and critical length of the shaft [8-11] have been extensively investigated. However, studies on the safety and stability of the shaft–tunnel intersection (STI) area of long-distance tunnels are limited.

Finding the analytical solution for three-dimensional stress distributions considering the intersection area of irregular and complex geometric shapes in the tunnel is impossible [12]. Studies have typically used numerical simulations to analyze the structural stability of irregular areas of tunnels. Existing numerical simulations analyzed the structural stability at the intersection of the tunnel and other buildings while taking into account the influence of geological factors [13], intersection angle [14], and other factors on regional stability.

The above study proved that the finite element calculation method can reflect the structural stability of the irregular area of the tunnel although it excludes the safety and stability analysis of the STI area. Compared with those of the common tunnel, the large difference in geological condition, ventilation shaft, and tunnel deformation and more complicated stress distribution of border area of structures in STI areas, which are usually located in a mountain, increases the difficulty in evaluating the security stability evaluation of general tunnel structures [14, 15]. Hence, structural safety assessment and design of the STI area are very challenging.

Therefore, field sampling and indoor sample methods were applied to a special operation tunnel to obtain the physical and mechanical parameters of the initial supporting structure. The vertical deformation, horizontal convergence, and maximum stress in the STI area are analyzed using the numerical simulation method. The stability of primary support and surrounding rock in the STI area is investigated by combining two evaluation indexes of allowable deformation and safety factors. The results of this study can provide a reference for future structural stability design and construction in the STI area of long-distance tunnels.

2. State of the art

The structural stability at the intersection of tunnels and other buildings has been extensively investigated. Elkadi and Huisman [16] developed a 3D subsurface geotechnical model in a 3D geoscientific information system (3D-GSIS) environment to explore the geomechanical performance of a tunnel boring machine through quantitative volumetric analysis. Hsiao et al. [13] adopted the numerical simulation

*E-mail address: yuyuanquan2010@126.com
ISSN: 1791-2377 © 2022 School of Science, IHU. All rights reserved.
doi:10.25103/jestr.152.19

method to examine the rock deformation of support design in tunnel intersection areas. A criterion for assessing the effect of intersection angles on tunnel behavior was established, and three categories of support design suggestions for different geological conditions were also proposed. Lin et al. [17] used FLAC3D to analyze the stability of the intersection of turbine and tailwater tunnel while focusing on the distribution of deformation, stress, plastic zone, and reinforcement system at the intersection of turbine and tailwater tunnel. Li et al. [15] explored the deformation and mechanical characteristics of tunnel lining in the tunnel intersection between the subway station and construction tunnels. The study showed that tensile and compressive failures may occur at the tunnel intersection and in a section 5 m away and locally thickening the supporting structures can improve the stability of the tunnel. Ramos Schneider et al. [18] presented innovative solutions for the intersection of the TBM tunnel and station that allow the construction of the tunnel and the later excavation of the station while maintaining the operation of the TBM and the tunnel lining. Lin et al. [14] examined the deformation behavior of existing tunnels caused by shield tunneling under the crossing with an oblique angle. The results showed that the transversal deformation and internal forces of the existing tunnel present evident asymmetrical characteristics due to the oblique intersection and an unrecoverable local torsional deformation of the existing tunnel on both sides of the new tunnel can be observed after shield tunneling. However, the maximum settlement of the existing tunnel crown is unaffected by the intersection angle. Zhang et al. [19] addressed the seismic responses of the cross-passage intersection using shaking table tests. Two simplified models are proposed to estimate joint extensions in a pseudo-static approach. Each model corresponds to a unique pattern of longitudinal deformation caused by discrepant responses of the intersection. Lai et al. [20] presented a special case study of a shield tunnel obliquely constructed close to an above-existing tunnel with a small intersection angle. Settlement characteristics of the existing tunnel were analyzed based on monitoring data and numerical simulations using the finite difference method (FDM). Field monitoring data indicated that the deformation of the existing tunnel caused by shield tunneling underneath is dominated by vertical settlement accompanied by torsional deformation. Sabagh and Ghalandarzadeh [21] conducted centrifugal modeling of continuous shallow tunnels at active normal fault intersection. The effects of fault displacement and tunnel collapse on the ground surface, including fault scarp, graben, and sinkhole, are observed and assessed. The existence of any of these surface features can be a potential risk for both surface and buried structures. Guo and Qu [1] investigated the stability control of the dynamic system of hydropower stations with two turbine units sharing a super long headrace tunnel (SLHT). The asymmetric governor parameters and load adjustments exert an effect on the stability of hydropower stations and the dynamic response processes (DRPs) of turbine frequencies. Miliziano et al. [22] predicted tunneling-induced effects by developing a three-dimensional numerical model that accounts for the complexities of the problem's geometry and construction phases.

The support design and stability of the tunnel crossing area [13, 15] considering the influence of geological factors [13], crossing angle [14, 20], and other factors on the deformation and stability of the tunnel structure at the crossing area have been thoroughly investigated. However, the current study considers simple geological conditions, and direct investigations on the structural stability of tunnel and shaft junctions are limited. The deformation and stress distribution of the interface area between ventilation shafts and tunnels are more complex than those of ordinary tunnels given that ventilation shafts of tunnels are usually located in high mountains and steep slopes with large differences in geological conditions, thereby increasing the difficulty in evaluating the safety and stability of ordinary tunnel structures [12, 23-25]. Meanwhile, finding an analytical solution for the three-dimensional stress distribution is impossible given the irregular and complex geometric shapes of the intersection area of the tunnel [12]. Numerical simulation is typically utilized to investigate the structural stability of irregular areas of the tunnel [14, 15, 17]. Therefore, this study aims to analyze the vertical deformation, horizontal convergence, and maximum stress at the junction of the ventilation shaft and tunnel through field sampling, indoor samples, and numerical simulation. The stability of the initial support and surrounding rock at the junction of the ventilation shaft and tunnel is then investigated by combining two evaluation indexes of allowable deformation and safety factors.

The remainder of this study is organized as follows. The general situation of the supporting project is described, physical and mechanical parameters of the supporting structure are obtained through laboratory tests, and the numerical analysis model of the STI area is established in Section 3. Stress, deformation, and the safety evaluation of the supporting structure in STI areas are discussed in Section 4. The conclusions are summarized in Section 5.

3. Methodology

3.1 Project Overview

The length of the left and right lines of a separate extra long tunnel in western China is 7285 and 7310 m, respectively, with a maximum buried depth of about 650 m. A shaft is set at the exit end to divide the left and right lines into three sections for feeding and exhausting mechanical ventilation. The depth of the shaft is approximately 258 m, and the total length of the four connecting air channels in the shaft is about 187 m. The left (right) STI area 1 is the position where the connection passage is connected to the left (right) tunnel at a smaller mileage, whereas the left (right) STI area 2 is the position where the connection passage is joined to the left (right) tunnel at a larger mileage. Analyzing the stability of primary support and surrounding rock is necessary given that only the primary support is used at the intersection area of four connecting air ducts and tunnels in the shaft. Understanding rock parameters is beneficial for decreasing the potential of geo-hazards during engineering works [26, 27]. Thus, extensive tests were carried out to obtain the physical and mechanical parameters of the surrounding rock of the STI area. Combined with engineering–geological and hydrogeological conditions of the site and referring to previous studies [27-30], the main factors that affect the primary support and surrounding rock stability in the STI area include primary support strength, primary support thickness, surrounding rock strength, tunnel buried depth, and other factors. In addition, the influence of mechanical ventilation of shafts on tunnel stability is negligible [13, 26, 30]. Thus, this factor is ignored in this study.

3.2 Parameters of supporting structure

(1) Test apparatus

The test was performed on the Rock 600-50 HT PLUS multifunctional triaxial Rock test system, as shown in Fig. 1. The system can conduct temperature–fluid–mechanical–chemical coupling tests of geological materials, such as rock. The maximum axial compressive load, confining pressure, and pore pressure are 1000 kN, 60 MPa, and 60 MPa (water or gas can be employed in the pore medium), respectively. The test temperature range of 0 – 90 °C can provide a variety of loading modes, such as flow, displacement, strain, and stress.

(a)

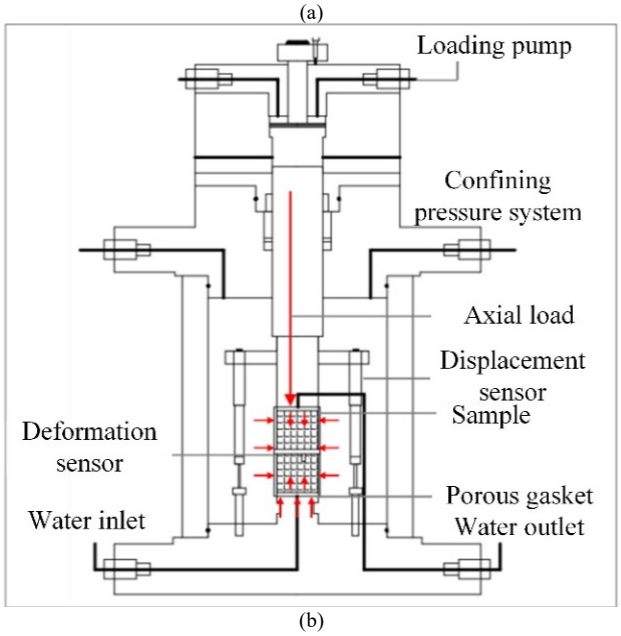

(b)

Fig. 1. Structure diagram of the test instrument: (a) test apparatus and (b) internal structure

(2) Test materials

Shotcrete core samples of primary support were obtained from the interface of each shaft connection passage. Core samples were further processed to create standard samples with a diameter of 50 mm and a height of 100 mm. Each group of tests contained three parallel tests.

(3) Test process

Three different confining pressure gradients of 2.0, 3.0, and 4.0 MPa and axial displacement control loading mode were used during the test. A loading rate of 1 MPa/min and hydrostatic pressure (σ2 = σ3) were applied to the predetermined confining pressure, while the confining pressure remained unchanged. The specific test process is presented as follows: (1) Place the sample into the rubber sleeve. (2) Place a metal permeable stone at both ends of the sample to reduce the stress concentration and avoid the hydraulic oil from flowing into the sample during the test and affecting the test results. (3) Use two linear displacement sensors (LVDT) to measure the axial strain, and calculate the circumferential strain with the circumferential electronic strain gauge placed in the height center of the sample.

(4) Test results

Fig. 2 shows the stress-strain curves of concrete at each position.

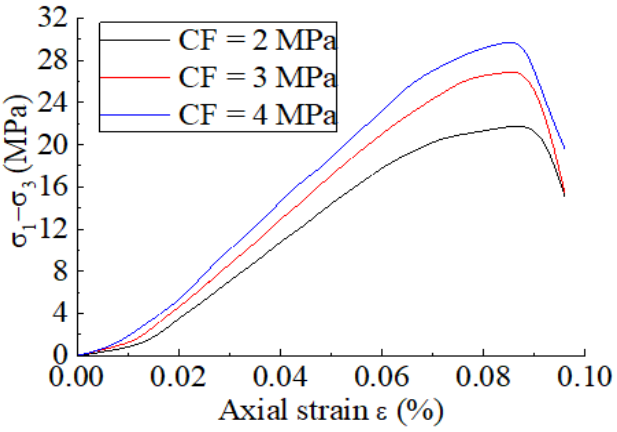

(a)

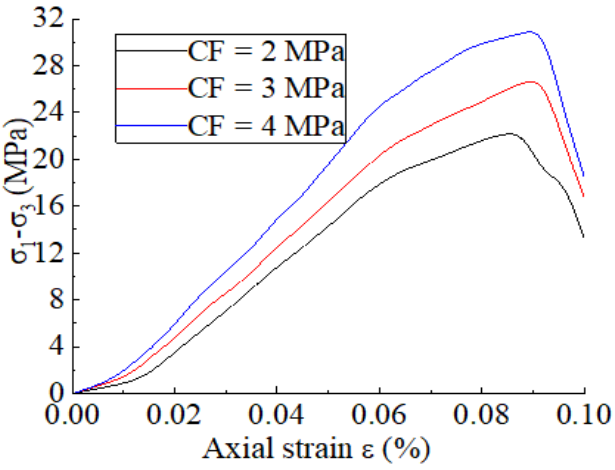

(b)

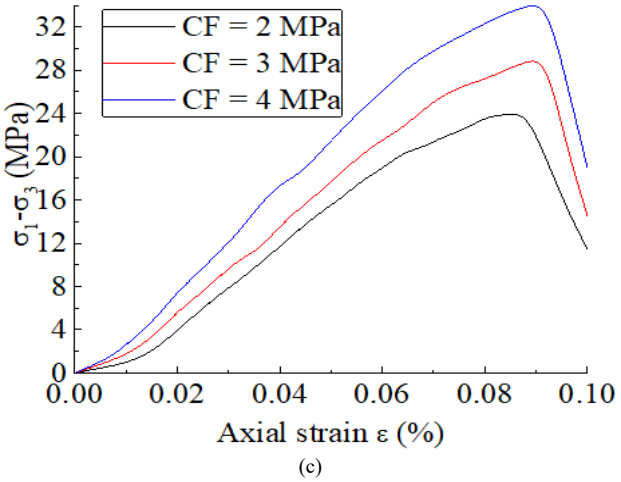

(c)

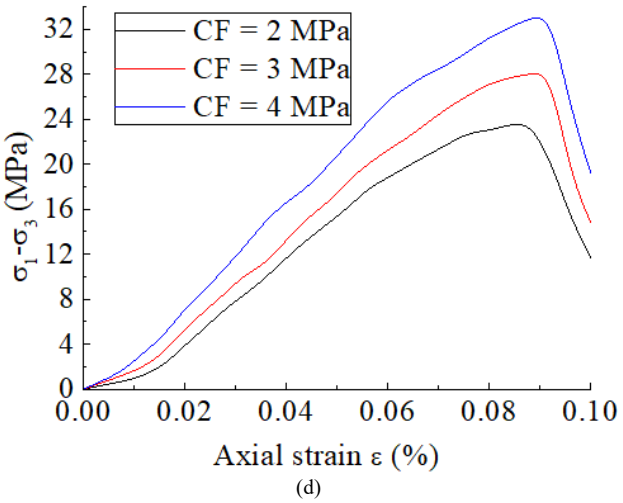

(d)

Fig. 2. Stress-strain curves of concrete samples at each STI area (CF is confining pressure): (a) left STI area 1, (b) left STI area 2, (c) right STI area 1, and (d) right STI area 2

According to the stress-strain curve, the concrete shows satisfactory linear elasticity before peak stress and the clear drop of strength after peak stress shows evident brittle failure. The stress-strain relationship of concrete under different confining pressures is similar, but the compressive strength of concrete increases slightly and the elastic modulus of concrete under different confining pressures are very similar to the increase of confining pressures.

The results of the conventional triaxial test of concrete are listed in Table 1. The test results showed that the compressive strength of concrete increases clearly with the increase of confining pressure. The actual compressive strength of concrete is higher than the design value in practical engineering because a higher buried depth indicates a higher stress level of the tunnel.

The value of σ1 is equal to the test value of concrete uniaxial compressive strength when σ3=0. The test values of concrete compressive strength at each location are listed in Table 2. The compressive strength of concrete cylinder specimens is generally 80%–85% of that of cube specimens [31-33]. The compressive strength of the C20 concrete cylinder is about 16.0–17.0 MPa.

Table 1. Results of conventional triaxial test of concrete

Group Number	Confining pressure, σ3 (MPa)	Axial pressure, σ1 (MPa)
Left STI area 1-1	2.0	23.9
Left STI area 1-2	3.0	29.1
Left STI area 1-3	4.0	33.9
Left STI area 2-1	2.0	24.3
Left STI area 2-2	3.0	29.9
Left STI area 2-3	4.0	35.2
Right STI area 1-1	2.0	26.1
Right STI area 1-2	3.0	32.1
Right STI area 1-3	4.0	38.3
Right STI area 2-1	2.0	25.7
Right STI area 2-2	3.0	31.2
Right STI area 2-3	4.0	37.3

Concrete thickness is measured directly during the coring process, the elastic modulus of concrete is obtained from stress-strain curves, and concrete Poisson's ratio is calculated from axial and circumferential strains.

Table 2. Concrete parameters at each position

Position	Elasticity modulus, E (MPa)	Poisson's ratio, μ	Thickness (cm)
Left STI area 1	24.8	0.18	32
Left STI area 2	25.2	0.20	32.5
Right STI area 1	25.9	0.21	30
Right STI area 2	25.5	0.19	33

The elastic modulus of concrete is between 25 and 26 MPa, and the standard elastic modulus of C20 concrete is 25.5 MPa. The actual elastic modulus of concrete is consistent with the standard elastic modulus. The average value of primary support thickness is 32 cm, which meets the design value of the on-site primary support thickness of 24 cm.

3.3 Numerical simulation analysis

(1) Calculation model and basic assumptions

The following are assumed: (1) The rock mass and support structure are isotropic bodies. (2) Stress and deformation characteristics of the connection passage are emphasized in the simulation; hence, the tunnel, shaft, and connection passage are excavated in one step, and the influence of construction on the connection passage is analyzed through displacement clearance. (3) Relative slip is absent between the supporting structure and rock mass. The symmetry of the established half model allowed the control of the number of model elements and improvement of computational efficiency. The numerical calculation model with dimensions of 165.4 m×74 m×102 m is shown in Fig. 3.

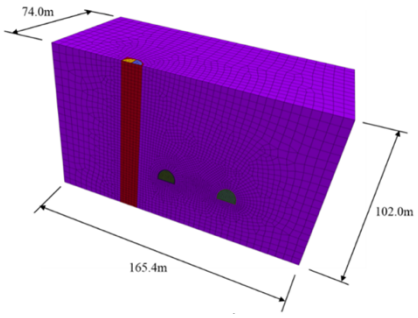

(a)

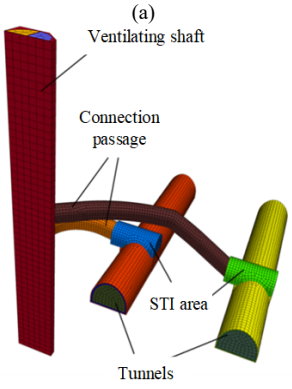

(b)

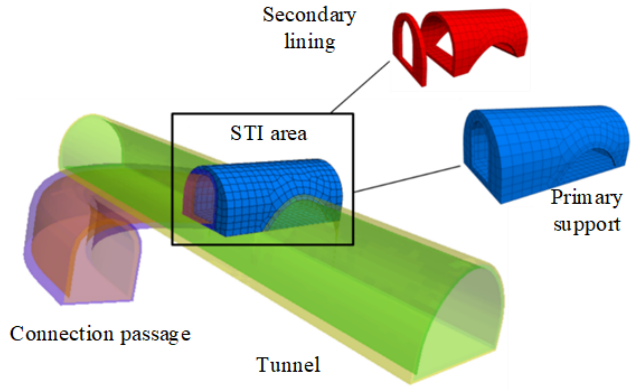

(c)

Fig. 3. Numerical calculation model: (a) size of the model, (b) shaft and connection passage, and (c) STI area

The bottom of the model is 30 m away from that of the tunnel, and this distance is more than four times the tunnel diameter to eliminate the boundary effect. The actual load was simulated by applying a load equal to the dead weight of the rock above the model surface. The rock above the upper surface of the model was about 220 m high. A uniform force of 5.61 MPa was applied to the upper surface of the model through numerical calculation, and the size of the numerical calculation model was finally established at 165.4 m×74 m×102 m (Fig. 3a). The fixed constraint was applied to the bottom of the model, and a horizontal displacement constraint was applied to the sides of the model. The top of the model was a free surface, and a uniform force of 5.61 MPa was applied. The model consists of 83202 nodes and 175009 units. Figs. 3b and 6c show the detailed structure of the shaft, connection passage, and the STI area.

(2) Calculation parameters

Mudstone is the main rock within the scope of the model, and the Mohr-Coulomb constitutive model is adopted for the rock. The primary support is C20 shotcrete, and the secondary lining is C25 reinforced concrete. The elastic constitutive model is adopted. The left line tunnel, the right line tunnel, and the shaft in the model all adopt the form of primary support and second lining. However, STI areas that only adopt the primary support are the most dangerous among the regions. Small values of primary support parameters of the left and right STI areas were selected with security consideration. The specific calculation parameters are listed in Table 3.

Table 3. Physical and mechanical parameters of rock and the supporting structure

Item	Thickness (m)	Unit weight, γ (kN/m3)	Elasticity modulus, E (GPa)	Poisson's ratio, μ	Cohesive force, c (MPa)	Internal friction angle, φ (°)	Tensile Strength, T (MPa)
Mudstone	-	25.5	1.8	0.35	0.35	25	4.0
Primary support of left STI area	0.24	25.0	26	0.18	-	-	-
Primary support of right STI area	0.24	25.0	26.8	0.19	-	-	-
Secondary lining	0.40	25.0	30	0.2	-	-	-

(3) Calculation conditions

Several groups of calculation conditions were compared to check the safety of STI areas when only the primary support is used, and the support effects were differentiated under various support parameters. The specific working conditions are presented in Table 4.

Table 4. Working conditions set in the STI areas

Condition	Thick of primary support (m)	Secondary Lining (m)	Remarks
1	0	0	Without support
2	0.12	0	-
3	0.24	0	Real condition of STI areas
4	0.24	0.2	-
5	0.24	0.4	The real condition of the initial design

(4) Calculation steps

MIDAS-GTS NX was utilized for auxiliary modeling and mesh division. Node and mesh information was then imported into FLAC3D 5.0 for calculation. The specific calculation steps are presented as follows: (1) Initial stress balance. (2) The displacement is cleared, and the excavation and support of the tunnel are carried out. The one-step excavation method is adopted, and the primary support and secondary lining are applied at the same time. (3) A one-step excavation method is adopted, and the support is applied. (4) The excavation and support of the connection passage are carried out, the one-step excavation method is adopted, and the primary support and secondary lining are simultaneously applied. (5) The displacement is zeroed out, and the excavation and support of STI areas are carried out. A one-step excavation method is adopted, and the primary support and the second lining are applied at the same time.

4. Result Analysis and Discussion

4.1 Stress and deformation analysis of the STI areas

(1) Vertical deformation

Fig. 4 illustrates the maximum vertical deformation diagram of STI areas under actual conditions (working condition 3). The vertical deformation is within 5 mm, and the maximum vertical deformation occurs in the vault and at the bottom of the arch, where no second lining is set in the STI area of the two tunnels. The sinking of the vault and rising of the bottom of the arch indicated that vertical deformation is affected by the absence of a secondary lining in the STI area. The limit vault displacement of primary support in the tunnel of the double-line tunnel with a buried depth of 300 m should be 0.4% H (tunnel height) [34]. The limit vault subsidence value at the STI area of 24 mm is significantly greater than that of the actual deformation. Therefore, using only the primary support in this part can meet the requirement of controlling the vertical deformation.

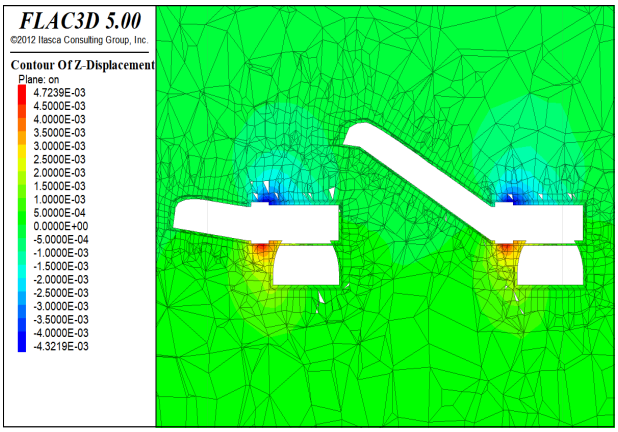

Fig. 4. Maximum vertical deformation profile of STI areas

Fig. 5 shows that the maximum vault settlement at STI areas under different working conditions is less than the allowable values. The maximum vault settlement of 11 mm for working condition 1 (without support) is significantly larger than that of other working conditions but still less than the limit vault subsidence value. However, STI areas should still be supported because the surrounding rock will be disturbed in the excavation process. The primary support with a thickness of 0.12 m should be adopted as the minimum support condition of working condition 2. The maximum vault settlement of working conditions 2–5 varies from 2 mm to 5 mm. Thus, the use of a 0.24 m-thick primary support is still safe in practical engineering.

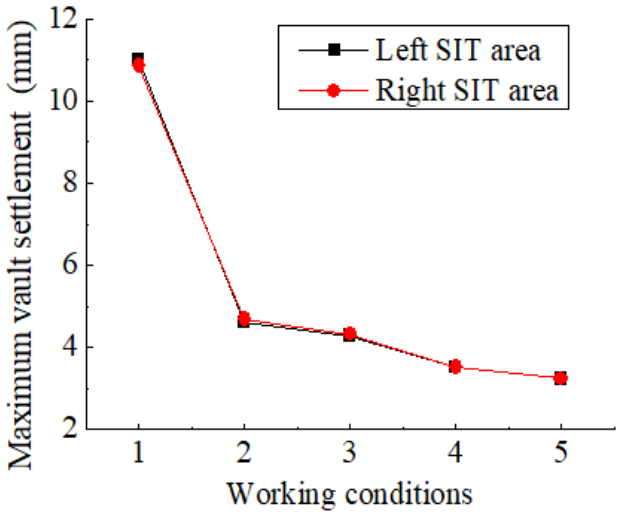

Fig. 5. Maximum vault settlement under different working conditions

(2) Horizontal convergence

Fig. 6 shows the horizontal convergence at STI areas under actual conditions. The maximum horizontal convergence of about 1.2 mm occurs at the arch shoulder of the two tunnel connectors where no second lining is set, with both directions moving toward the tunnel. This finding showed that the horizontal convergence in STI areas is affected to some extent. The limit horizontal convergence of primary support in the tunnel of the double-line tunnel with a buried depth of 300 m should be 0.96% D (D is the net distance of the tunnel) [34]. The limit horizontal convergence of 76.8 mm is significantly larger than that of the actual deformation. Therefore, using only the primary support in this part can meet the requirements of controlling horizontal convergence.

Fig. 7 illustrates the maximum horizontal convergence of STI areas under different working conditions. Moreover, the maximum horizontal convergence in STI areas under different working conditions is less than the limit horizontal convergence of 76.8 mm. The maximum horizontal convergence for working condition 1 (without support) is approximately 10 mm, which is significantly larger than that of other working conditions but still less than the limit horizontal convergence. The minimal difference between the maximum horizontal convergences of STI areas under working conditions 2 to 5 is within 2 mm. The horizontal convergence is effectively controlled after the lining is applied, and using a 0.24 m-thick primary support is safe in practical engineering.

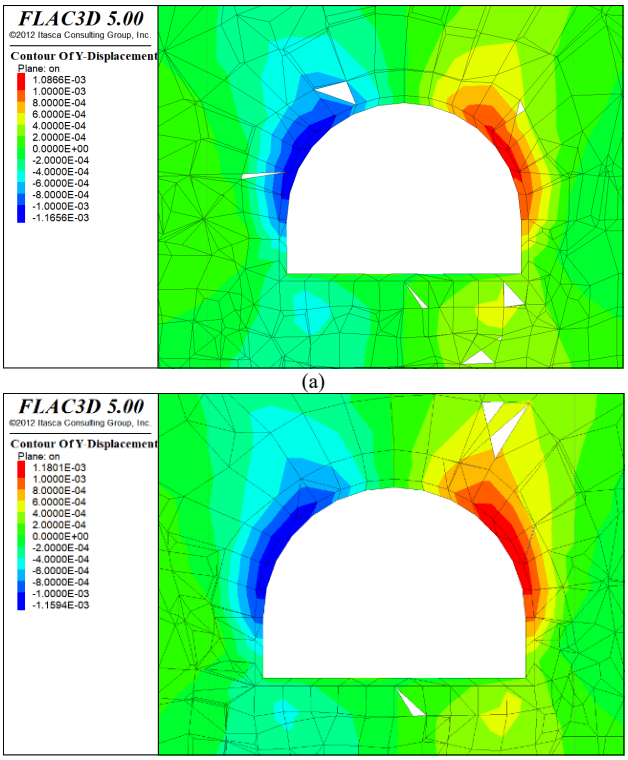

Fig. 6. Horizontal convergence of STI areas: (a) left and (b) right STI areas

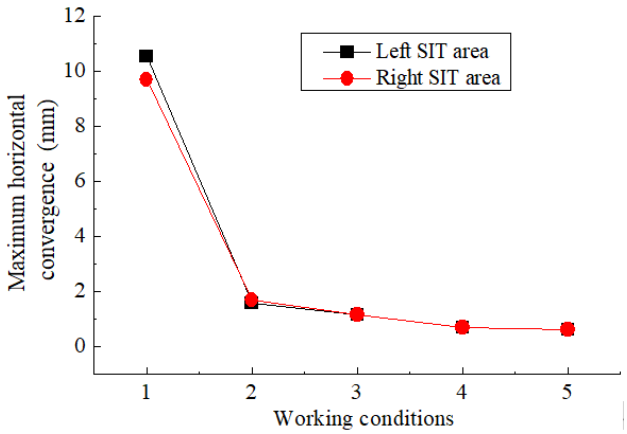

Fig. 7. Maximum horizontal convergence of STI areas under different working conditions

(3) Maximum stress

The maximum stresses of the concrete lining at STI areas were calculated to consider the stress state of the supporting structure further (Table 5). Stress levels of the concrete lining at the left and right STI areas are very close, with a maximum tensile stress of 0.82 and 0.87 MPa and maximum

compressive stress of 0.83 and 0.74 MPa, respectively. The strength of the test concrete is used for verification, and small values of the two connecting ports of the left and right sides of the tunnel are presented as follows: The design tensile strengths of the concrete lining in the left and right STI areas are 9.2 and 10.1 MPa, respectively. The tensile strength is generally one-eighth the value of the compressive strength. The maximum tensile stresses of the primary concrete lining in the left and right STI areas are 71.3% and 69.0% of the design value of concrete tensile stress, respectively. The primary support is still in safety. The maximum compressive stresses of the primary concrete lining in the left and right STI areas at 9.02% and 7.33% of the design value of concrete compressive stress, respectively, are small and not used as the control parameter for the safety of the primary support.

Table 5. Table of the maximum stress of concrete lining

Area	Maximum tensile stress (MPa)	Maximum compressive stress (MPa)	The design value of concrete tensile (compressive) stress (MPa)	Maximum tensile (compressive) stress level (%)
Left STI area	0.82	0.83	1.15 (9.2)	71.3 (9.02)
Right STI area	0.87	0.74	1.26 (10.1)	69.0 (7.33)

The maximum stresses of primary concrete lining in STI areas under different working conditions are shown in Fig. 8. The tensile stress of the primary concrete lining under the five working conditions is less than or equal to the design value of the concrete tensile strength, thereby indicating that the primary concrete lining is in safety. The stress level of primary concrete lining in the right STI area is greater than that in the left STI area mainly because the right STI area is far from the shaft, the connection passage is longer, and thus the primary support plays a greater role. The load it bears increases and the stress level increases continuously with the increase of the thickness of the primary support under working conditions 1–3. The additional stress on the primary support begins to decrease under working condition 4 because the secondary lining is involved in the support and part of the load is borne by the secondary lining. Only a 0.24 m-thick primary support is used in practical engineering. Although the primary support bears large tensile stress, it remains within the safe range.

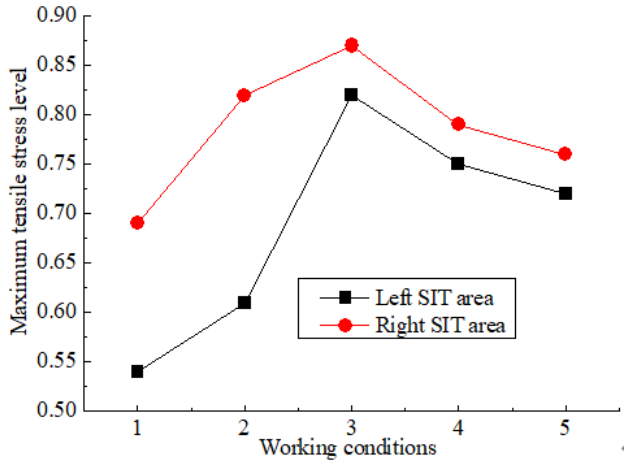

Fig. 8. Maximum tensile stress level of primary support under different working conditions

4.2 Safety evaluation and analysis of the supporting structure of the STI areas

As stated in section 4.1 the allowable subsidence value of the tunnel vault is 24 mm for this project. In addition, another safety factor of the supporting structure in the tunnel during the construction period is proposed by Zhou [35] based on the deformation of the support structure; thus, the relationship between the safety of the tunnel support structure and its displacement can be established. The safety evaluation of primary support and surrounding rock stability in STI areas can be carried out by integrating the two evaluation indexes of allowable deformation and safety factors. Fig. 9 shows the limit of structural safety displacement in the STI areas, in which the allowable value of horizontal convergence of the arch shoulder is 76.8 mm and that of the arch foot is 64 mm.

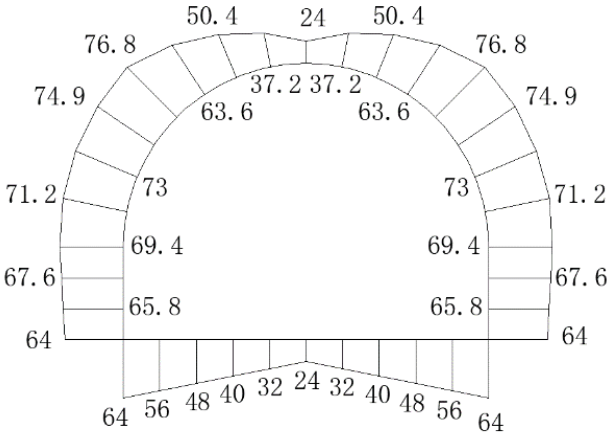

Fig. 9. Limit of structural safety displacement at STI areas

The total displacement cloud diagram of the support structure at STI areas under various working conditions was extracted to reflect the total displacement level around the STI areas under different supporting conditions, as shown in Fig. 10 (working condition 3 is used as an example). The total displacement of the supporting structure at the STI area under working condition 3 is less than 4.58 mm, which is significantly lower than that of the structural safety displacement limit at the STI area.

Only the safety factor diagrams of the maximum deformed section in the STI area under working conditions 1 and 3 are presented in Figs. 11 and 12, respectively, given that safety factors of the STI area under working conditions 4 and 5 are significantly greater than those of the STI area under working conditions 1–3.

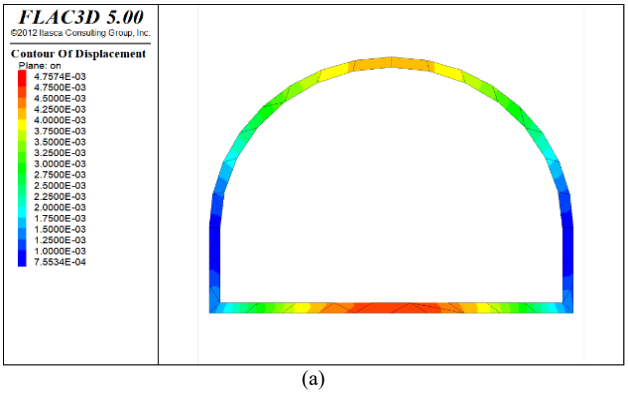

(a)

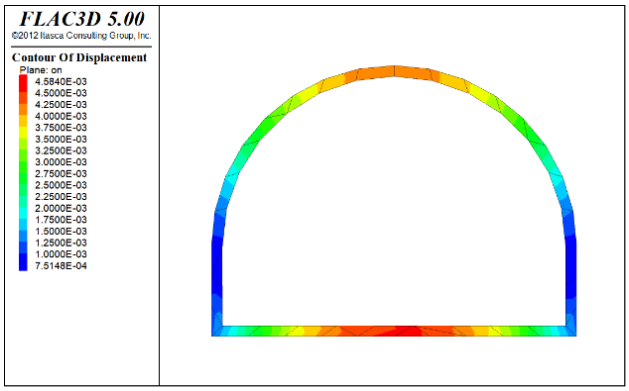

(b)

Fig. 10. The total displacement of supporting structure at STI areas (working condition 3): (a) left and (b) right STI areas

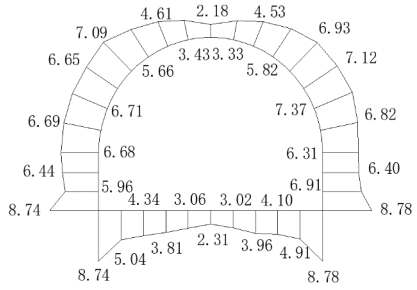

(a)

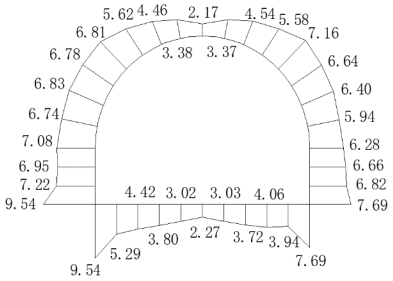

(b)

Fig. 11. Diagram of the safety factor in the STI area under working condition 1: (a) left and (b) right STI areas

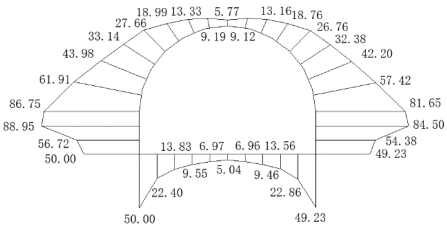

(a)

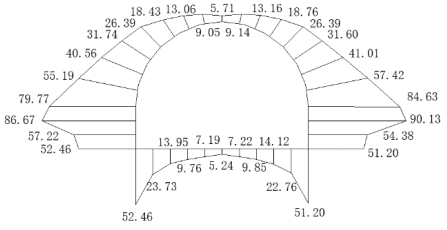

(b)

Fig. 12. Diagram of the safety factor in the STI area under working condition 3: (a) left and (b) right STI areas

As shown in Figs. 11 and 12, the overall distribution of the safety factor in the STI area under the working conditions is the minimum at the tunnel vault and arch bottom but large at the tunnel arch waist because the limit convergence value is large and the lateral pressure of the surrounding rock is small at the tunnel arch waist. Thus, the tunnel vault and arch bottom are the key parts for security control. According to the code in Reference [34], the strength safety factor of reinforced concrete structure should be greater than or equal to 2.4 when the concrete reaches the ultimate tensile strength and the safety factor of deformation control should also refer to the safety factor stipulated in the code. The tunnel arch and bottom safety coefficients under working condition 1 in the left STI area are 2.18 and 2.31 and those in the right STI area are 2.17 and 2.27, respectively. These values are all lower than the safety coefficients specified in the code. Therefore, the excavated tunnel needs to be supported to meet the design requirements. Safety coefficients of the maximum deformation sections in the left and right STI areas under working conditions 2–5 are all greater than 4; hence, the requirements of the specification are met. The minimum safety factor of the tunnel section can still reach 5.04 even if a 0.24 m-thick primary support is used in the actual situation. The design of the primary support is still safe and appropriate because of its location at the arch bottom of the maximum deformation section in the left STI area and larger value than the specified one with a large surplus.

5. Conclusions

The vertical deformation, horizontal convergence, and maximum stress in the STI areas were analyzed using laboratory testing and numerical simulation to evaluate the stability of the STI area accurately and implement corresponding treatment measures. The structural stability in the STI area was also examined. The following conclusions can be drawn from this study:

(1) The triaxial test results showed that the compressive strength of the concrete cylinder in the primary support reaches approximately 16.0 – 17.0 MPa, which is around 80 – 85% of the standard strength value of C20 concrete. The primary support of concrete can meet the requirements of compressive strength.

(2) The average thickness of the primary support in the STI area is about 32 cm, which is higher than the design value of 24 cm. The maximum vertical deformation is less than 5 mm and the horizontal convergence is less than 2 mm; thus, deformations are within the allowable range. The maximum concrete tensile and compressive stress levels of the primary support in the left and right STI areas are 71.3% and 69.0%, respectively.

(3) The use of primary support with a thickness of 24 cm can ensure that the minimum safety factor of the tunnel section reaches 5.04, which is greater than the specified value with a large surplus. Therefore, the design of the primary support is appropriate. The minimum safety factor of the support structure in the STI area will be greater than 5.04 given that the actual average thickness of the primary support can reach about 32 cm. The actual thickness of the primary support can ensure the safety of the STI area under the current conditions.

The structural stability of the STI area is simulated in this study to analyze the force, deformation, and stability of the STI area. The results of this study can provide a reference for the structural stability analysis of similar STI areas. However, monitoring data will be compared and corrected with the numerical simulation results proposed in this study in a future investigation given the lack of

monitoring information on structural deformation in the STI area for comparison to improve the accuracy of the structural stability evaluation in STI areas.

Acknowledgments

This study was supported by the Science and Technology Project of the Chongqing Education Commission (No. KJQN201802301).

This is an Open Access article distributed under the terms of the Creative Commons Attribution License.

References

1. Guo, W., Qu, F., "Stability control of dynamic system of hydropower station with two turbine units sharing a super long headrace tunnel". *Journal of the Franklin Institute*, 358(16), 2021, pp. 8506-8533.
2. Qian, C., Chen, J., Luo, Y., Zhao, Z., "Monitoring and analysis of the operational environment in an extra-long highway tunnel with longitudinal ventilation". *Tunnelling and Underground Space Technology*, 83(1), 2019, pp. 475-484.
3. Zhang, Z., Zhang, H., Tan, Y., Yang, H., "Natural wind utilization in the vertical shaft of a super-long highway tunnel and its energy saving effect". *Building and Environment*, 145(11), 2018, pp. 140-152.
4. Deng, M., "Challenges and Thoughts on Risk Management and Control for the Group Construction of a Super-Long Tunnel by TBM". *Engineering*, 4(1), 2018, pp. 112-122.
5. Wu, G., Chen, W., Bian, H., Yuan, J., "Structure optimisation of a diaphragm wall with special modelling methods in a large-scale circular ventilating shaft considering shield crossing". *Tunnelling and Underground Space Technology*, 65(5), 2017, pp. 35-41.
6. Sanada, H., Sato, T., Horiuchi, Y., Mikake, S., Okihara, M., Yahagi, R., Kobayashi, S., "Excavation cycle times recorded during sinking of a deep shaft in crystalline rock – A case example at Ventilation Shaft of Mizunami URL, Japan". *Tunnelling and Underground Space Technology*, 50(8), 2015, pp. 68-78.
7. Zhang, S., He, K., Yao, Y., Peng, M., Yang, H., Wang, J., Cheng, X., "Investigation on the critical shaft height of plug-holing in the natural ventilated tunnel fire". *International Journal of Thermal Sciences*, 132(10), 2018, pp. 517-533.
8. Xu, Z., Xu, W., He, L., Xie, E., Wang, T., Tao, H., "Numerical study on the smoke extraction efficiency and the improvement through a smoke reservoir in the naturally ventilated tunnel with vertical shaft". *Tunnelling and Underground Space Technology*, 103(9), 2020, pp. 103505.
9. Guo, Q., Zhu, H., Zhang, Y., Yan, Z., "Theoretical and experimental studies on the fire-induced smoke flow in naturally ventilated tunnels with large cross-sectional vertical shafts". *Tunnelling and Underground Space Technology*, 99(5), 2020, pp. 103359.
10. Yao, Y., Li, Y. Z., Ingason, H., Cheng, X., "Numerical study on overall smoke control using naturally ventilated shafts during fires in a road tunnel". *International Journal of Thermal Sciences*, 140(6), 2019, pp. 491-504.
11. He, K., Cheng, X., Zhang, S., Yao, Y., Peng, M., Yang, H., Cong, W., Shi, Z., Chen, Z., "Experimental study on smoke control using wide shafts in a natural ventilated tunnel". *Journal of Wind Engineering and Industrial Aerodynamics*, 195(12), 2019, pp. 104015.
12. Chen, C. N., Tseng, C. T., "2D tunneling chart from redistributed 3D principal stress path". *Tunnelling and Underground Space Technology*, 25(4), 2010, pp. 305-314.
13. Hsiao, F. Y., Wang, C. L., Chern, J. C., "Numerical simulation of rock deformation for support design in tunnel intersection area". *Tunnelling and Underground Space Technology*, 24(1), 2009, pp. 14-21.
14. Lin, X. T., Chen, R. P., Wu, H.-N., Cheng, H. Z., "Deformation behaviors of existing tunnels caused by shield tunneling undercrossing with oblique angle". *Tunnelling and Underground Space Technology*, 89(7), 2019, pp. 78-90.
15. Li, Y., Jin, X., Lv, Z., Dong, J., Guo, J., "Deformation and mechanical characteristics of tunnel lining in tunnel intersection between subway station tunnel and construction tunnel". *Tunnelling and Underground Space Technology*, 56(6), 2016, pp. 22-33.
16. Elkadi, A. S., Huisman, M., "3D-GSIS geotechnical modelling of tunnel intersection in soft ground: the Second Heinenoord Tunnel, Netherlands". *Tunnelling and Underground Space Technology*, 17(4), 2002, pp. 363-369.
17. Lin, P., Zhou, Y., Liu, H., Wang, C., "Reinforcement design and stability analysis for large-span tailrace bifurcated tunnels with irregular geometry". *Tunnelling and Underground Space Technology*, 38(9), 2013, pp. 189-204.
18. Ramos Schneider, G., Garcia-Fontanet Molina, A., Torralba Mendiola, V., Ainchil Lavin, J., "Innovative solutions for intersection of TBM tunnel and station in Riyadh Line 5 metro". *Tunnelling and Underground Space Technology*, 80(10), 2018, pp. 26-37.
19. Zhang, J., Yuan, Y., Bao, Z., Yu, H., Bilotta, E., "Shaking table tests on the intersection of cross passage and twin tunnels". *Soil Dynamics and Earthquake Engineering*, 124(9), 2019, pp. 136-150.
20. Lai, H., Zheng, H., Chen, R., Kang, Z., Liu, Y., "Settlement behaviors of existing tunnel caused by obliquely under-crossing shield tunneling in close proximity with small intersection angle". *Tunnelling and Underground Space Technology*, 97(3), 2020, pp. 103258.
21. Sabagh, M., Ghalandarzadeh, A., "Centrifugal modeling of continuous shallow tunnels at active normal faults intersection". *Transportation Geotechnics*, 22(3), 2020, pp. 100325.
22. Miliziano, S., Caponi, S., Carlaccini, D., de Lillis, A., "Prediction of tunnelling-induced effects on a historic building in Rome". *Tunnelling and Underground Space Technology*, 119(1), 2022, pp. 104212.
23. Vitali, O. P. M., Celestino, T. B., Bobet, A., "3D face effects of tunnels misaligned with the principal directions of material and stress anisotropy". *Tunnelling and Underground Space Technology*, 122(4), 2022, pp. 104347.
24. Hu, Z., Shen, J., Wang, Y., Guo, T., Liu, Z., Gao, X., "Cracking characteristics and mechanism of entrance section in asymmetrically-load tunnel with bedded rock mass: A case study of a highway tunnel in southwest China". *Engineering Failure Analysis*, 122(4), 2021, pp. 105221.
25. Alhawat, H., Hamid, R., Baharom, S., Azmi, M. R., Kaish, A. B. M. A., "Thermal behaviour of unloaded concrete tunnel lining through an innovative large-scale tunnel fire experimental testing setup". *Construction and Building Materials*, 283(5), 2021, pp. 122718.
26. Fraldi, M., Cavuoto, R., Cutolo, A., Guarracino, F., "Stability of tunnels according to depth and variability of rock mass parameters". *International Journal of Rock Mechanics and Mining Sciences*, 119(7), 2019, pp. 222-229.
27. Tiwari, G., Pandit, B., Gali, M. L., Babu, G. L. S., "Analysis of Tunnel Support Requirements Using Deterministic and Probabilistic Approaches in Average Quality Rock Mass". *International Journal of Geomechanics*, 18(4), 2018.
28. Xu, J., Ni, Y., "Displacement ratio dichotomy back analysis of surrounding rock-initial support system of weathered rock tunnel". *Arabian journal of geosciences*, 12(6), 2019.
29. Kim, J. Y., Kim, K. Y., "Effects of vent shaft location on the ventilation performance in a subway tunnel". *JOURNAL OF WIND Engineering and Industrial Aerodynamics*, 97(5-6), 2009, pp. 174-179.
30. Xu, S., *Shotcrete Support of a Ventilation Shaft in Hard Rock*, in *Civil Engineering, Architecture and Sustainable Infrastructure II, Pts 1 and 2*. 2013. p. 1133-1136.
31. Muciaccia, G., Rosati, G., Di Luzio, G., "Compressive failure and size effect in plain concrete cylindrical specimens". *Construction and Building Materials*, 137(4), 2017, pp. 185-194.
32. Kaish, A. B. M. A., Jamil, M., Raman, S. N., Zain, M. F. M., "Axial behavior of ferrocement confined cylindrical concrete specimens with different sizes". *Construction and Building Materials*, 78(3), 2015, pp. 50-59.
33. Yazıcı, Ş., İnan Sezer, G., "The effect of cylindrical specimen size on the compressive strength of concrete". *Building and Environment*, 42(6), 2007, pp. 2417-2420.

34. TB10003-2016, "Code for Design of Railway Tunnel". *Industrial standard of the People's Republic of China*, 2016.

35. Zhou, Y., "R*esearch on excavation methods and supporting structure system of tunneling schemes in crushed phyllite*". Master thesis of Southwest Jiaotong University, 2014.